Supplement of Geosci. Model Dev., 19, 8855–8876, 2026
https://doi.org/10.5194/gmd-19-8855-2026-supplement

Geoscientific Model Development
Open Access

Supplement of

Evaluation of plume rise parameterizations in GEM-MACHv2 with analysis of image data using a deep convolutional neural network

Kevin M. Axelrod et al.

Correspondence to: Mark Gordon (mgordon@yorku.ca)

S1. Analysis of variance in plume rise with modified parameters.

Figures S1 through S3 present the results of several sensitivity analyses for the criteria we used to filter ensemble data from section 3.2 of the main text to obtain plume rise measurements that are representative of bent-over plumes that are correctly identified as such by the DCNN. For each of the analyses presented, one single criterion is varied per section – all other criteria remain what was used for section 3.2 in the main text.

Figure S1 displays a sensitivity analysis in which average plume rise is calculated based on the range of wind directions that are accepted when eliminating images with associated wind directions that are in line with the camera orientation (the plane of 162° and/or 342°). The wind direction cutoff angle in the plot is the angle from the camera orientation line (i.e. between the red and green lines in Fig. 5). A larger wind direction cutoff indicates that a larger range either above or below those two wind directions is eliminated from the ensemble, hence the number of qualifying images decreases with increasing cutoff angle. Both the Briggs-predicted plume rise and the DCNN-analyzed plume rise show a decrease as more wind directions are eliminated. This is expected, as images with wind directions that are closer to the camera orientation are more likely to result in large values. The ratio of Briggs to DCNN plume rise is relatively constant over a wide range of cutoff angles. Here we choose a 45° cutoff angle to include the bulk of westerly winds (Fig. 5) and because this allows a range of wind angles that is large in comparison to the wind direction uncertainty (~25° as discussed in Section 3.5.1).

Figure S2 presents a sensitivity analysis in which the allowed pixel range between the start point of the plume and the average location on the image of the main stack exit point is varied, and resulting variation in plume rise is plotted. At a small allowable pixel range (<25 pixels) the plume rise is relatively high but there are relatively few qualifying images. The number of qualifying images increases rapidly as the accepted range increases from 25 to 50 pixels, and then it increases at a slower rate for pixel ranges above 50 pixels. Overall, plume rise increases as the pixel range increases but begins to decrease after the pixel range is increased above 150 pixels and is in fact at its highest (both DCNN and Briggs) when the pixel range is small, though that is with significantly fewer qualifying images. The ratio of Briggs to DCNN plume rise is relatively constant for cutoff values above 50 pixels, so this value is chosen as the cutoff pixel box size.

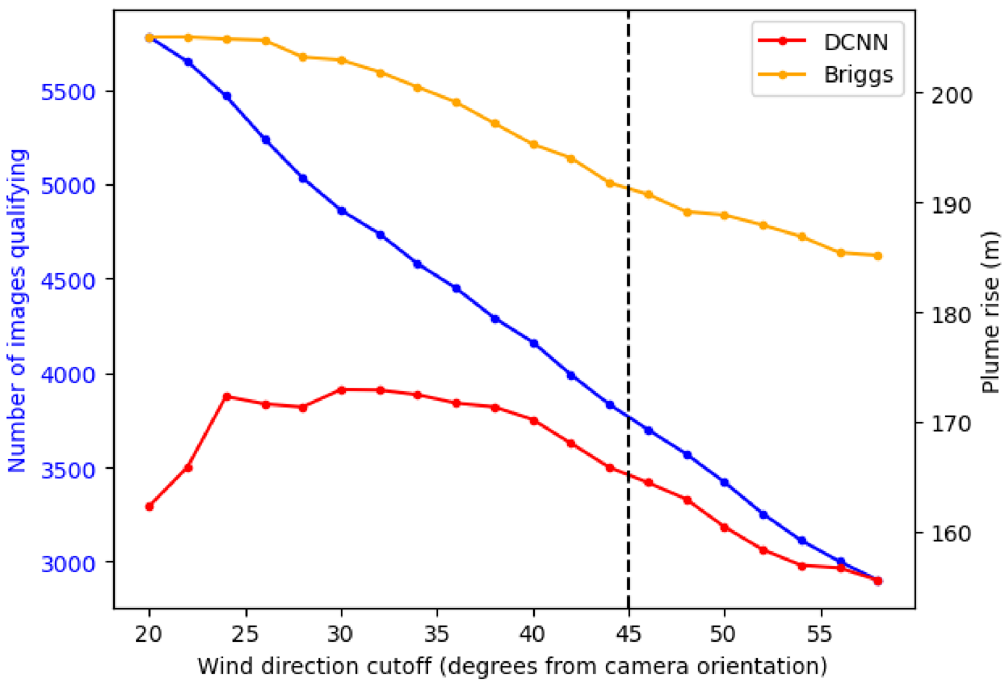

Figure S1. Variation in plume rise (both DCNN-analyzed and Briggs-predicted) and number of images qualifying for analysis with variation in selected cutoff for wind direction relative to camera angle. Figures with corresponding wind speed data (from AMS03 100m sensor) less than the wind speed indicated from the x-axis are not used in the calculation of Δh.

Figure S3 presents a separate analysis in which 22 plumes that appeared vertical in orientation were manually selected from the ensemble image set, in addition to 53 plumes that appeared bent-over in orientation. This selection of images differs from the manually-selected set analyzed in Section 3.2, as plumes are selected to include a variety of vertical and bent-over plumes. To further differentiate bent-over and vertical plumes, we took the slope of the horizontal midpoint line of each plume identified by the DCNN (vertical pixel rise over horizontal pixel distance). In examining the wind speed from the 100m sensor of AMS03, we found that 82% of vertical plumes had wind speeds lower than 3 m s^{-1}, and 83% of bent-over plumes had wind speeds higher than 3 m s^{-1}.

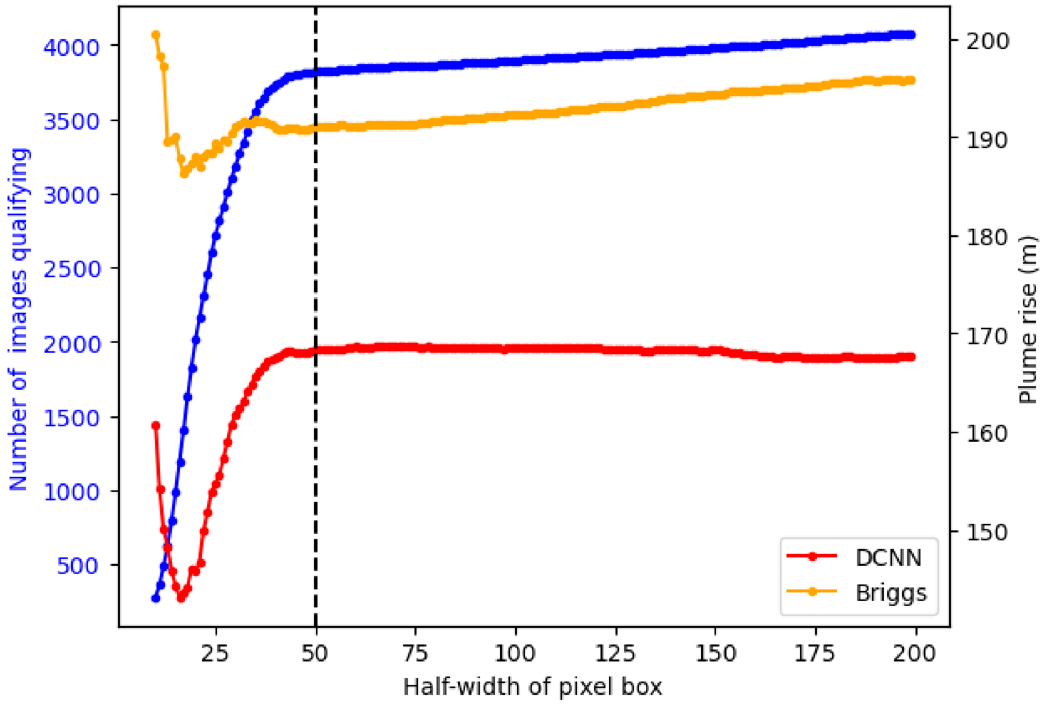

Figure S2. Variation in plume rise (both DCNN-analyzed and Briggs-predicted) and number of images qualifying for analysis with size of box (in pixel x and y dimension) on image within which plume start points must lie within.

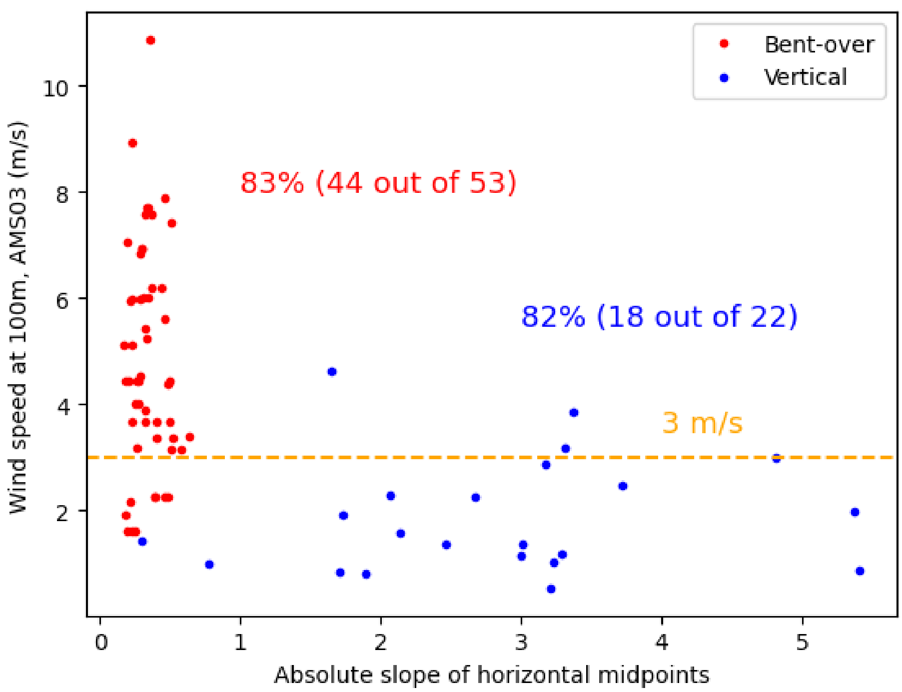

Figure S3. Wind speed and linear slope of horizontal midpoint lines of several manually-selected vertical and horizontal plumes from the ensemble image set (not the same manually-selected set analyzed in Section 3.2), with the fitted linear slope of their horizontal midpoint lines on the x axis and the associated wind speed from WBEA's AMS03 100m sensor.

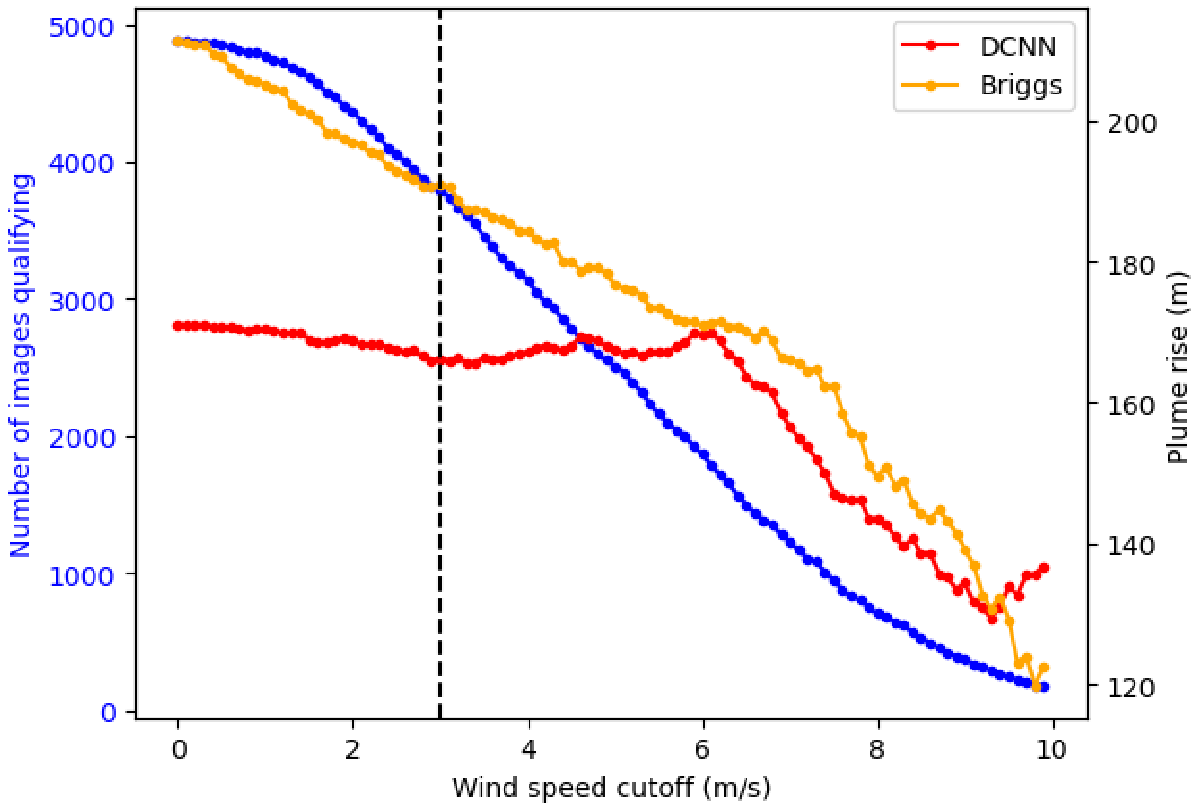

Figure S4. Variation in plume rise (both DCNN-analyzed and Briggs-predicted) and number of images qualifying for analysis with variation in selected cutoff for minimum wind speed cutoff. Figures with corresponding wind speed data (from AMS03 100m sensor) less than the wind speed indicated from the x-axis are not used in the calculation of Δh.

Figure S4 presents a sensitivity analysis in which the minimum wind speed cutoff is varied. This was performed to determine if there was a minimum wind speed that correctly separated out vertical plumes (which would have resulted in a high plume rise in our analysis) from bent-over plumes. Unsurprisingly, the number of qualifying images decreased as the minimum speed criteria was increased, and furthermore, both the DCNN-analyzed and the Briggs-predicted plume rise decreased – indicating that lower wind speed from AMS03's sensor correlates with plumes with a more bent-over shape. However, as the criteria resulted in fewer images being analyzed, there was more variation in the DCNN-analyzed plume rise from point-to-point, which indicates that there is higher variability in DCNN-analyzed plume rise measurements. The ratio of Briggs to DCNN plume rise decreases with cutoff wind speeds up to 6 m/s, after which it is relatively constant. Here we choose a cutoff value of 3 m/s as a balance between selecting bent-over plumes only versus including an adequate number of plumes for the analysis, although we do recognize that modifying this value will likely have an effect on the Briggs to DCNN comparison.

S2. Examples of plumes and associated DCNN-generated image masks.

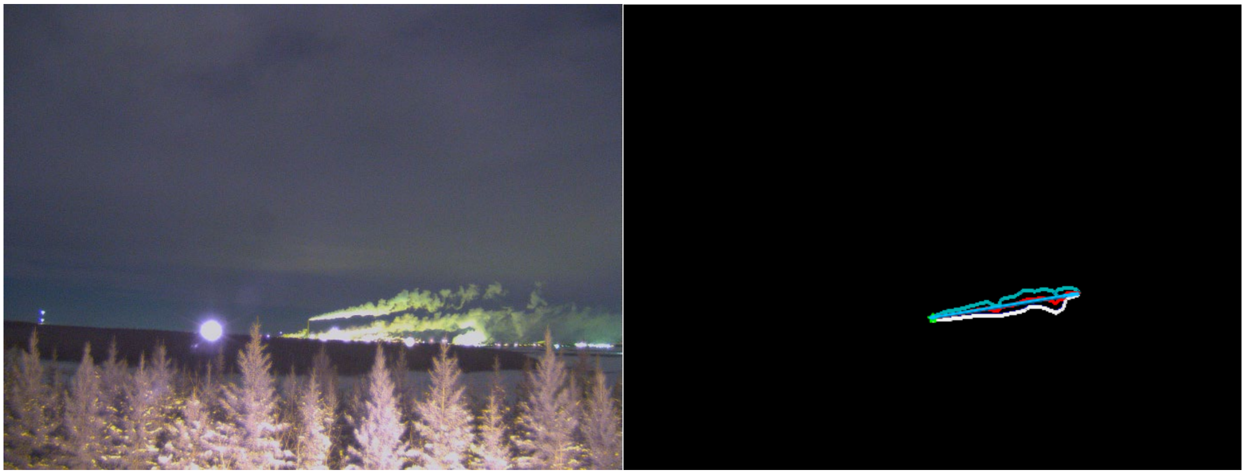

Figure S5. In this image, the midline of the plume is interpreted as a near-straight diagonal line. The exponential fit of this line has an asymptote that would lie more than 175000 pixels above the top edge of the image (i.e. 90 times the image height of 1944 pixels). The plume rise distance in pixels would lie more than 519000 pixels to the right of the right edge of the image (i.e. 192 times the image width of 2592 pixels).

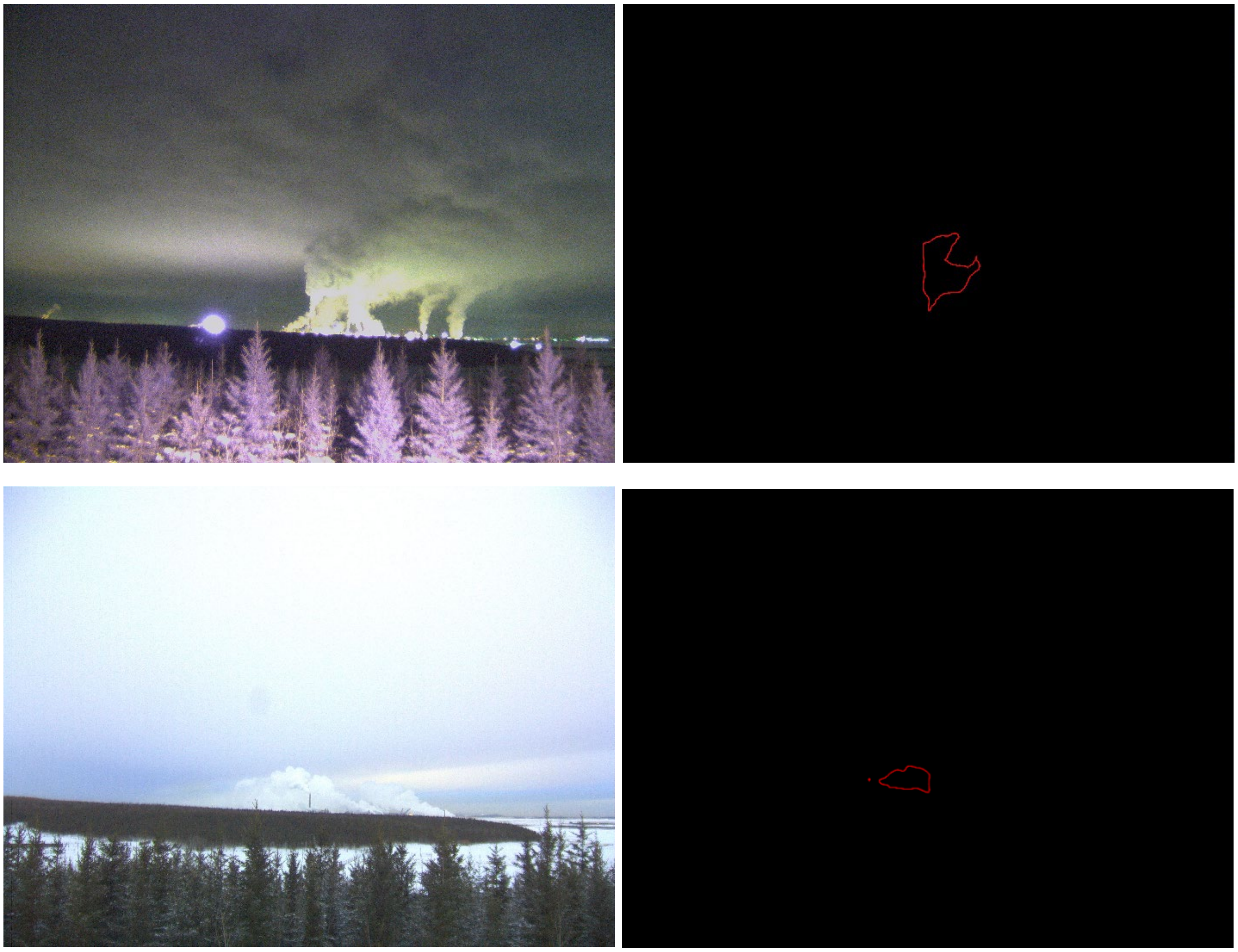

Figure S6. Examples of plumes drifting towards (top) and away from (bottom) the camera

Figures S7. Examples of plumes in which the DCNN did not accurately trace out the visible plume structure. A) Instance of vertical plume not fully identified. B) Instance of additional plume from Mildred Lake Coker being included in Main Stack plume. C). Instance where other plumes and surrounding clouds make plume identification difficult.

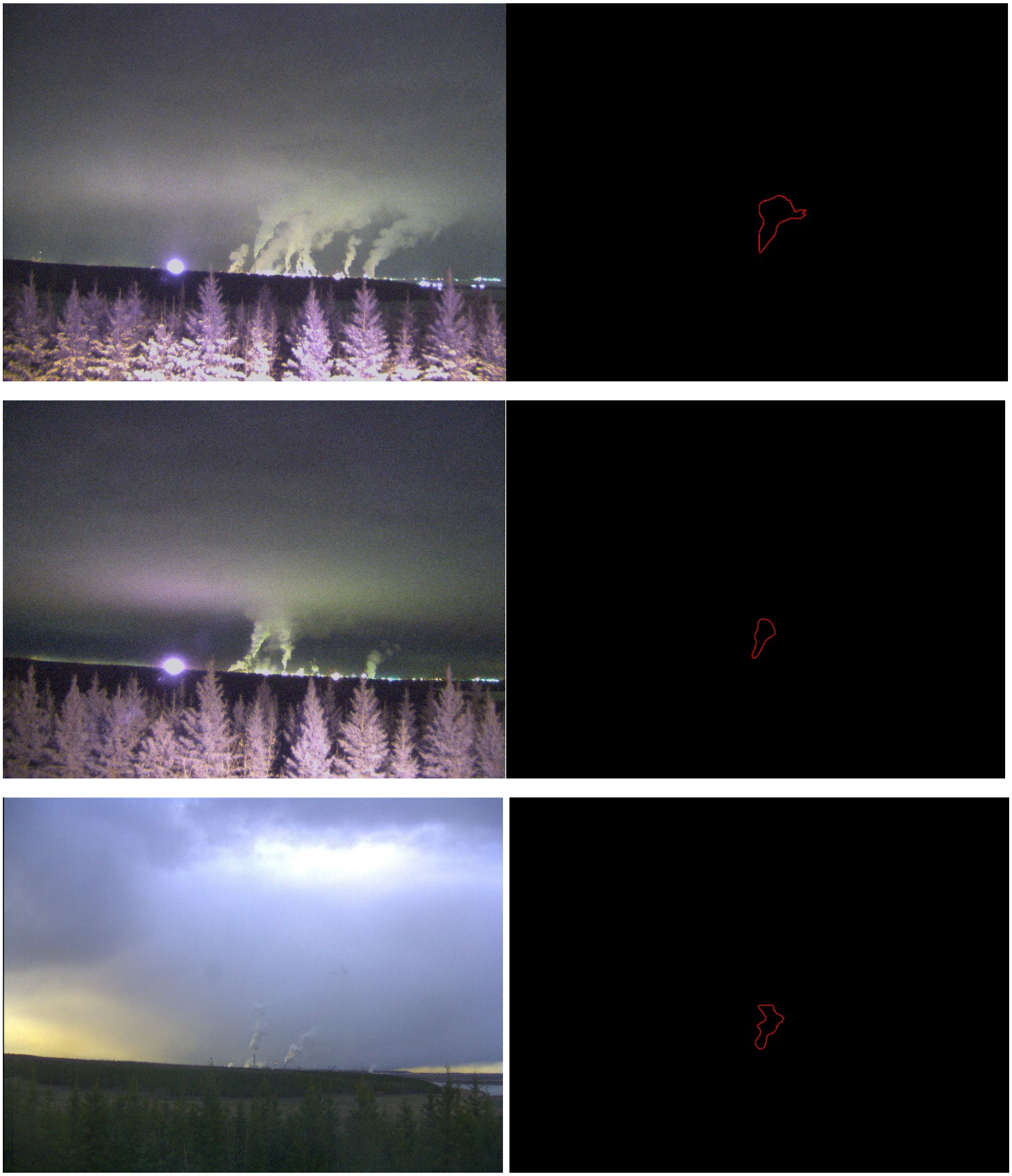

Figure S8. Plumes that are primarily vertical in orientation as observed by camera.

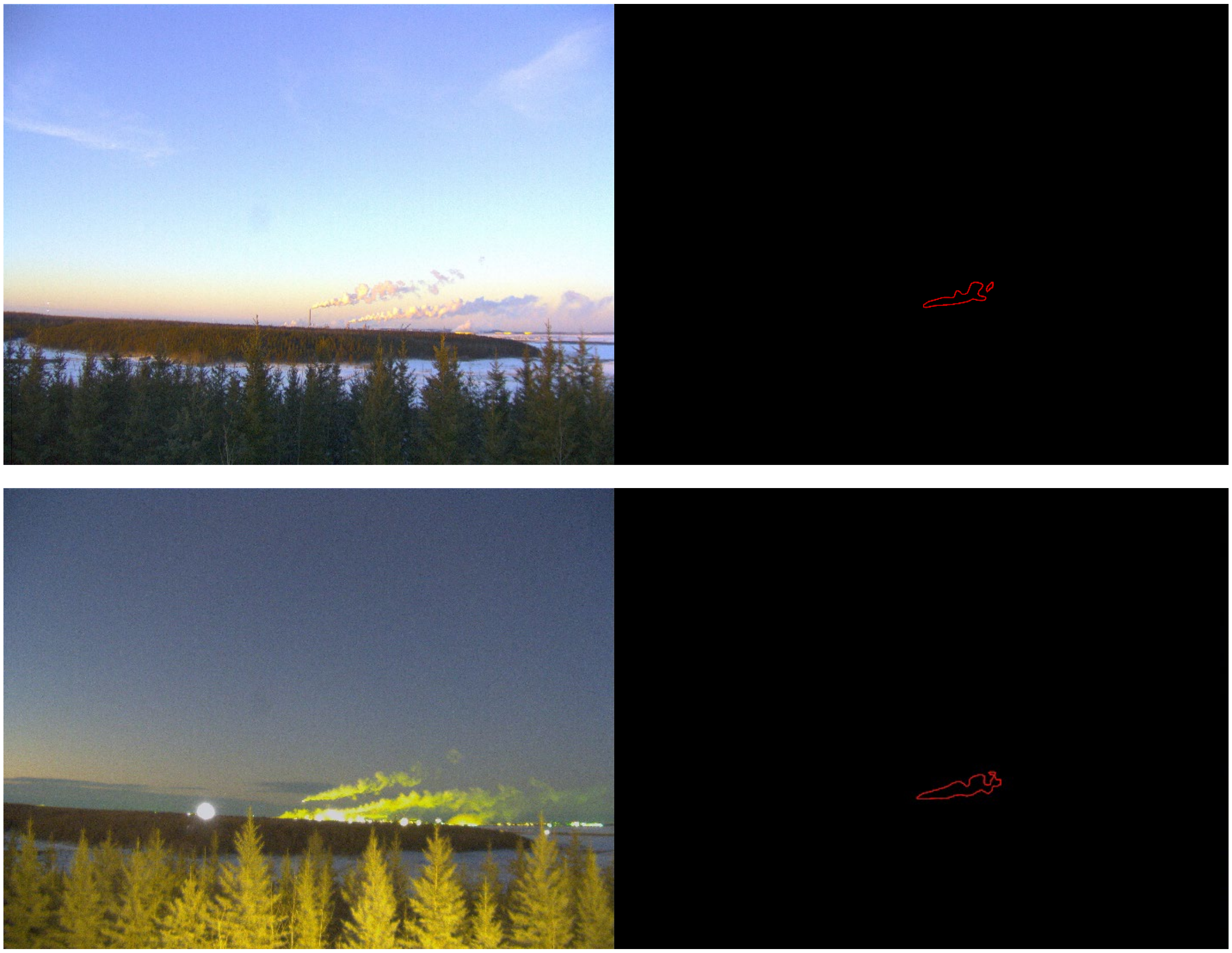

Figure S9. Example of segmented plume with broken and separated clouds. Only the main portion of the cloud is identified by the DCNN.

S3. Geometric Transformation of Plume Rise.

Section 2.2 conceptually outlines the geometric transformation required to convert the locations of the smokestack and neutral buoyancy point within the image to a physical plume rise value using the wind direction and the properties of the camera. This derivation (originally outlined in Koushafar et al., 2023), was developed independently of the more generalized derivation from Snee et al. (2023), which accounts for camera tilt angle. Here, the camera is mounted level and that correction is not required. These equations have been verified against those of Snee et al. (2023).

The given variables are the measured wind direction, which is used to calculate the angle θ, the distance between the camera and the image plane, D (determined from satellite imagery and GPS coordinates), and the pixel locations of the stack and neutral buoyancy points within the image (x_s, y_s and x_p, y_p respectively), measured from the image centre, positive to the right and upward in the image. From the known camera focal length, field of view, array size, and D, we can determine the physical dimension of each pixel in the image plane, δ (m/px).

Using this information with the view from above shown in Figure S13, we can determine the following set of equations

$$OS_h = x_s\delta,$$

$$OP'_h = x_p\delta,$$

$$\tan a = OP'_h/D, \tag{S1}$$

$$\tan\theta = OO'/(O'P_h - OS_h),$$

$$\tan a = O'P_h/(D + OO')$$

Solving this set of equations for $O'P_h$ and OO'_h in terms of the known values gives

$$O'P_h = x_p\delta\left(1 - \frac{x_s\delta}{D}\tan\theta\right)/\left(1 - \frac{x_p\delta}{D}\tan\theta\right) \tag{S2}$$

$$OO'_h = (O'P_h - x_s\delta)\tan\theta \tag{S3}$$

From these values, we can calculate the horizontal plume rise distance as

$$D_p = \sqrt{(O'P_h - x_s\delta)^2 + (OO')^2} \tag{S4}$$

Similarly, the view from the side gives

$$OS_v = y_s\delta,$$

$$OP'_v = y_p\delta, \tag{S5}$$

$$\tan b = OP'_v/D,$$

$$\tan b = O'P_v/(D + OO'_v)$$

Solving this set of equations for $O'P_v$ in terms of the known values gives

$$O'P_v = \frac{y_p\delta}{D}(OO' + D), \tag{S6}$$

which is used to determine vertical plume rise as

$$\Delta z = O'P_v - OS_v. \quad \text{(S7)}$$

Figure S10 demonstrates the configuration for $0 < \theta < 90^{\circ}$, corresponding to a wind blowing the plume towards the right in the image and further away from the camera. When the angle is $-90^{\circ} < \theta < 0$, the plume will move to the right of the image and towards the camera. In this case, the values of OO' will be negative, but there is no required change to the equations (since $\tan\theta < 0$). Similarly, when winds are from the east and the plume moves to the left of the image ($-180^{\circ} < \theta < -90^{\circ}$ or $90^{\circ} < \theta < 180^{\circ}$), the values of x_p, $O'P_h$, and OP_h' will all be negative, but the solution is the same since $\tan\theta = \tan(\theta + 180°)$.

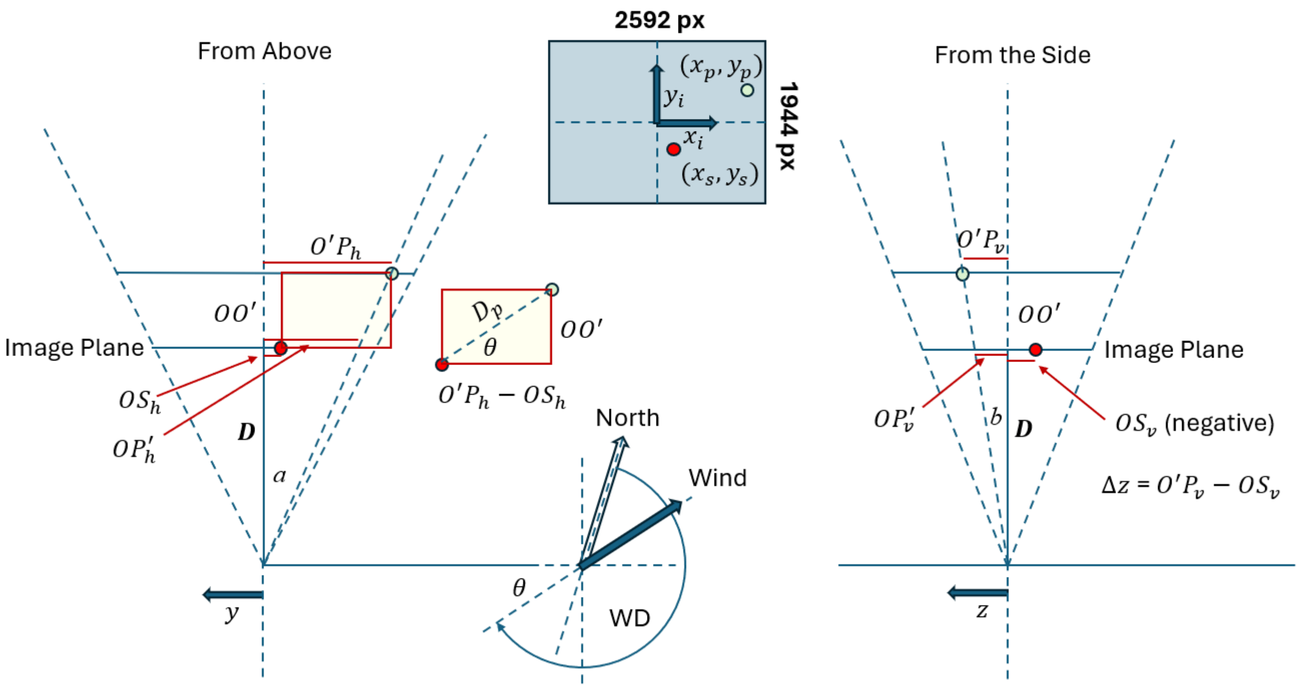

Figure S10. Schematic of geometric transformation to determine horizontal plume rise distance (D_p) and vertical plume rise (Δz). The schematic corresponds to Fig. 3 but is shown here with wind from the SW quadrant. The stack exit location (red dot) and plume location (green dot) are shown in the image corresponding to the image space (with axes, x_i and y_i), and physical space with views in x-y (from above) and x-z (from the side). We show the stack location slightly below the image centre (corresponding to our actual setup), which means that $y_s < 0$. which gives a negative value for length for OS_v.